catalysts

MDPI

Article

Abundant Oxygen Vacancies Induced by the Mechanochemical Process Boost the Low-Temperature Catalytic Performance of MnO_2 in NH_3-SCR

Yuanyuan Dong [1,2], Baofang Jin [2,*], Shaomian Liu [2], Jiajian Gao [3,*], Kangjun Wang [1,4,*] and Fabing Su [2,4]

1 Key Laboratory of Resources Chemicals and Materials, Shenyang University of Chemical Technology, Ministry of Education, Shenyang 110142, China
2 State Key Laboratory of Multiphase Complex Systems, Institute of Process Engineering, Chinese Academy of Sciences, Beijing 100190, China
3 Institute of Sustainability for Chemicals, Energy and Environment, Agency for Science, Technology and Research (A*STAR), 1 Pesek Road, Jurong Island, Singapore 627833, Singapore
4 Institute of Industrial Chemistry and Energy Technology, Shenyang University of Chemical Technology, Shenyang 110142, China
* Correspondence: jinbaofang@ipe.ac.cn (B.J.); gao_jiajian@isce2.a-star.edu.sg (J.G.); wangkj_dut@syuct.edu.cn (K.W.)

Abstract: Manganese oxides (MnO_x) have attracted particular attention in the selective catalytic reduction of NO_x with NH_3 (NH_3-SCR) because of their excellent low-temperature activity. Herein, we prepared a highly efficient MnO_2 (MnO_2-M) catalyst through a facile ball milling-assisted redox strategy. MnO_2-M shows a 90% NO_x conversion in a wide operating temperature window of 75–200 °C under a gas hourly space velocity of 40,000 h^{-1}, which is much more active than the MnO_2 catalyst prepared by the redox method without the ball-milling process. Moreover, MnO_2-M exhibits better H_2O and SO_2 resistance. The enhanced catalytic properties of MnO_2-M originated from the high surface area, abundant oxygen vacancies, more acid sites, and higher Mn^{4+} content induced by the ball-milling process. In situ DRIFTS studies probed the reaction intermediates, and the SCR reaction was deduced to proceed via the typical Eley–Rideal mechanism. This work provides a facile method to enhance the catalytic performance of Mn-based catalysts for low-temperature denitrification and deep insights into the NH_3-SCR reaction process.

Keywords: MnO_2; ball-milling; high surface area; oxygen vacancies; low-temperature NH_3-SCR

check for updates

Citation: Dong, Y.; Jin, B.; Liu, S.; Gao, J.; Wang, K.; Su, F. Abundant Oxygen Vacancies Induced by the Mechanochemical Process Boost the Low-Temperature Catalytic Performance of MnO_2 in NH_3-SCR. *Catalysts* **2022**, *12*, 1291. https://doi.org/10.3390/catal12101291

Academic Editors: Fan Lin and Jong-Ki Jeon

Received: 22 September 2022
Accepted: 19 October 2022
Published: 21 October 2022

1. Introduction

One of the most significant factors causing environmental pollution is NO_x emitted by burning fossil fuels, leading to a series of environmental concerns such as ozone depletion, acid rain, and photochemical smog [1,2]. At present, selective catalytic reduction by NH_3 (NH_3-SCR) is one of the effective technologies to reduce NO_x [3–5], typically using the V_2O_5-WO_3/TiO_2 and V_2O_5-MoO_3/TiO_2 catalysts [6,7]. However, the V-based catalysts have some disadvantages, e.g., the narrow working temperature window and biological toxicity. Additionally, their operating temperature is required to be above 300 °C, which is energy-consuming [8,9]. Therefore, it is essential to develop novel non-V-based SCR catalysts with high activity at low temperatures [10–12].

Mn-based catalysts have been widely investigated for low-temperature NH_3-SCR due to their high catalytic activity, good redox properties, relatively low toxicities, and low cost [13,14]. In the case of pure MnO_x catalysts, their different valence states typically affect the catalytic activity. Yang et al. [15] found that MnO_2 exhibited higher NO conversion at 75–250 °C than Mn_2O_3 and Mn_3O_4 because of the higher valence state of Mn in MnO_2. In addition, the crystallinity and surface area of MnO_x can also affect its catalytic performance. Tang et al. [16] found that amorphous MnO_x with a higher specific area had higher activity

than highly crystallized MnO_x. Moreover, the NH_3-SCR reaction involves the participation of reactive oxygen species, e.g., NO oxidation to NO_2. Oxygen vacancies (OVs) are also helpful in improving the catalytic activity of MnO_x [17]. For example, Liu et al. [18] reported that mesoporous α-MnO_2 nanosheets with more OVs reached 100% NO conversion under a gas hourly space velocity (GHSV) of 700,000 h^{-1} at 100 °C.

Several strategies have been developed to generate OVs in metal oxides. For example, Chen et al. [19] employed aqueous $NaBH_4$ to reduce Co_3O_4, and OVs were generated during the surface reduction process. Sun et al. [20] found that the post-acid-etching process effectively made OVs in MnO_x. Hilpert et al. [21] prepared $LaCrO_{3-\delta}$ with many OVs by exposing $LaCrO_3$ to oxidizing and reducing atmospheres under 900–1100 °C operating conditions. Yim et al. [22] used ion sputtering and annealing reduction method to obtain rutile TiO_2 with high OVs concentration. Although these approaches have proven effective, they are relatively complicated and costly. Increasing the OVs concentration of MnO_x through simple and economical alternative routes to improve its catalytic performance is essential but challenging.

Herein, we report a facile ball milling-assisted redox strategy to obtain a high-performing MnO_2 catalyst (MnO_2-M) by introducing abundant OVs. In contrast to the MnO_2 catalyst obtained by the conventional redox method (MnO_2), MnO_2-M exhibits much higher activity in the NH_3-SCR reaction. This is mainly attributed to the abundant OVs, more acid sites, and higher Mn^{4+} content induced by the ball-milling process. The corresponding structure-activity relationship and reaction mechanism was elucidated by investigating the catalyst structure in detail. This work demonstrates significant progress for the practical applications of pure MnO_x in NO_x elimination at low temperatures.

2. Results and Discussion

2.1. Characterization of the Catalysts

2.1.1. XRD and PSD Analysis

Figure 1a shows the XRD patterns of the catalysts. In the pattern of MnO_2-M, three prominent diffraction peaks appear at 37.5°, 42.0°, and 57.0°, which can be indexed as the (211), (301), and (431) planes of α-MnO_2 (PDF#44-0141), respectively [23]. Compared with the MnO_2-M catalyst, MnO_2 shows more diffraction peaks. These diffraction peaks match well with the standard pattern of the α-MnO_2 phase (PDF#44-0141), where the stronger diffraction peaks at 2θ = 28.8°, 37.5°, and 42.0° can be ascribed to the (310), (211), and (301) planes of the MnO_2, respectively [24,25]. It should be noted that the XRD pattern of the MnO_2-M catalyst shows significantly broadened diffraction peaks with poor crystallinity, indicating that its crystal growth is suppressed during the ball milling-assisted redox process. Indeed, M-MnO_2 obtained by the ball-milling of MnO_2 for 1 h also presents lower crystallinity and smaller particle size, indicating that the ball-milling process does affect the structure of the catalyst. The crystal sizes of the MnO_2-M catalyst based on the Debye–Scherrer equation calculated from the strongest diffraction peak at 2θ = 37.5° is 4.92 nm, while that at 2θ = 28.8° calculated at 27.17 nm for the MnO_2 catalyst (Table 1). The particle size of the catalysts was measured using a laser particle size analyzer, and the results are shown in Figure 1b. The size of MnO_2 is centered at 1–20 μm. However, the MnO_2-M catalyst has different distributions at 0.2–2, 2–6, and 6–20 μm, suggesting that both small and large particles coexist. The mixture of particles with different sizes benefits the formation of inter-particle pores.

2.1.2. N_2 Adsorption Measurements

The BET surface area and total pore volume of the catalysts are listed in Table 1. The MnO_2-M catalyst possesses a larger surface area (177.9 vs. 66.4 m^2/g) and pore volume (0.335 vs. 0.149 cm^3/g) than the MnO_2 catalyst. The larger surface area may be because the MnO_2-M catalyst contains abundant inter-particle pores, which can also be deduced from the PSD results. To interpret such a difference, the N_2 adsorption–desorption isotherms and pore size distribution of the two catalysts are also shown in Figure 2. The two catalysts

display the type IV adsorption isotherms with H3-type hysteresis, indicating the formation of a porous structure [26]. As seen in Figure 2b, the pore size distributions of the two catalysts obtained from nitrogen adsorption are both in the range of 5–30 nm. However, the peak intensity of the pore size distribution in the MnO_2-M catalyst is much higher than in the MnO_2 catalyst, which means that more pores, including large and small sizes, exist in the MnO_2-M catalyst.

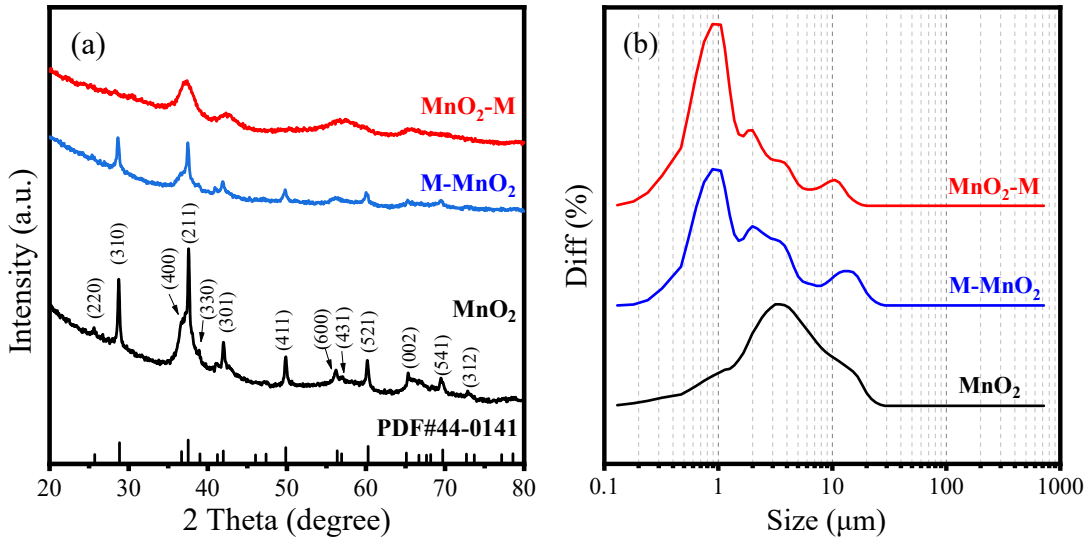

Figure 1. XRD patterns (**a**) and PSD curves (**b**) of the catalysts.

Table 1. Physical properties of the catalysts.

Catalyst	S_{BET} [i] ($m^2\ g^{-1}$)	V_P [ii] ($cm^3\ g^{-1}$)	Lattice Parameter [iii] (Å)		Average Crystallite Size [iv] (nm)
			a = b	c	
MnO_2-M	177.9	0.335	9.7904	2.8544	4.92
MnO_2	66.4	0.149	9.8156	2.8561	27.17

[i] Surface area derived from the BET equation. [ii] Pore volume was obtained from the volume of nitrogen adsorbed at a relative pressure of 0.99. [iii] XRD results for the MnO_2 phase in the catalysts, calculated by the Bragg equation. [iv] Estimated from the XRD diffraction peak (2θ = 37.5° for MnO_2-M and 28.8° for MnO_2) using the Debye–Scherrer equation.

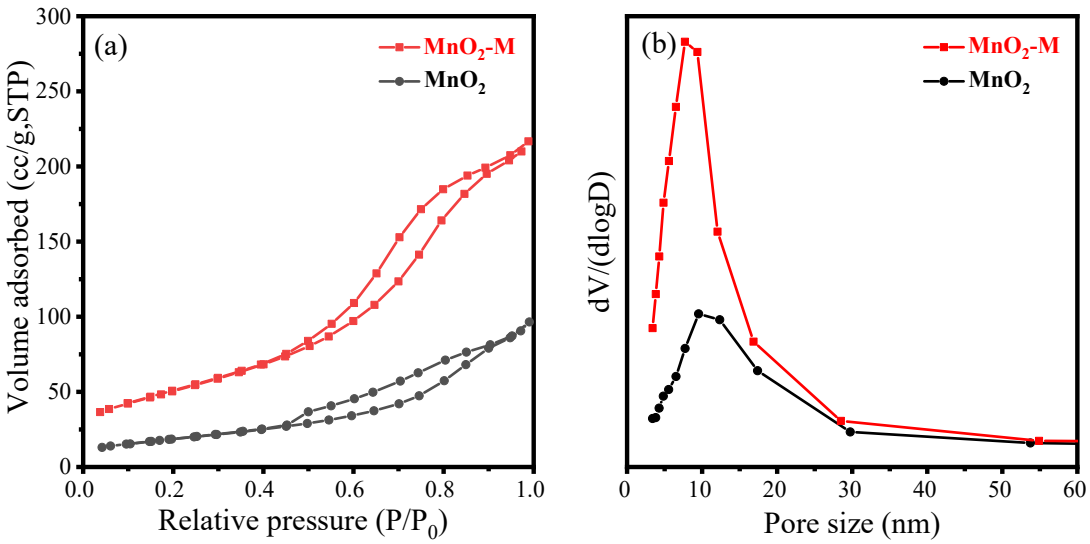

Figure 2. N_2 adsorption-desorption isotherms (**a**) and pore size distribution curves (**b**) of the catalysts.

2.1.3. SEM Observation

Figure 3 depicts the typical SEM images of MnO_2-M and MnO_2. The MnO_2-M catalyst exhibits irregular particles of varying sizes, while the MnO_2 catalyst displays a unique waxberry-like shape with consistent dimensions. Compared with the MnO_2 catalyst containing particles in close contact, the particles in the MnO_2-M catalyst are in loose connection, which is more conducive to forming inter-particle pores. This is also evidenced by the PSD result (Figure 1b) and N_2 adsorption result (Figure 2). In short, inter-particle pores can increase the specific surface area of the catalyst and provide more active sites between the catalyst and gas-phase reactants.

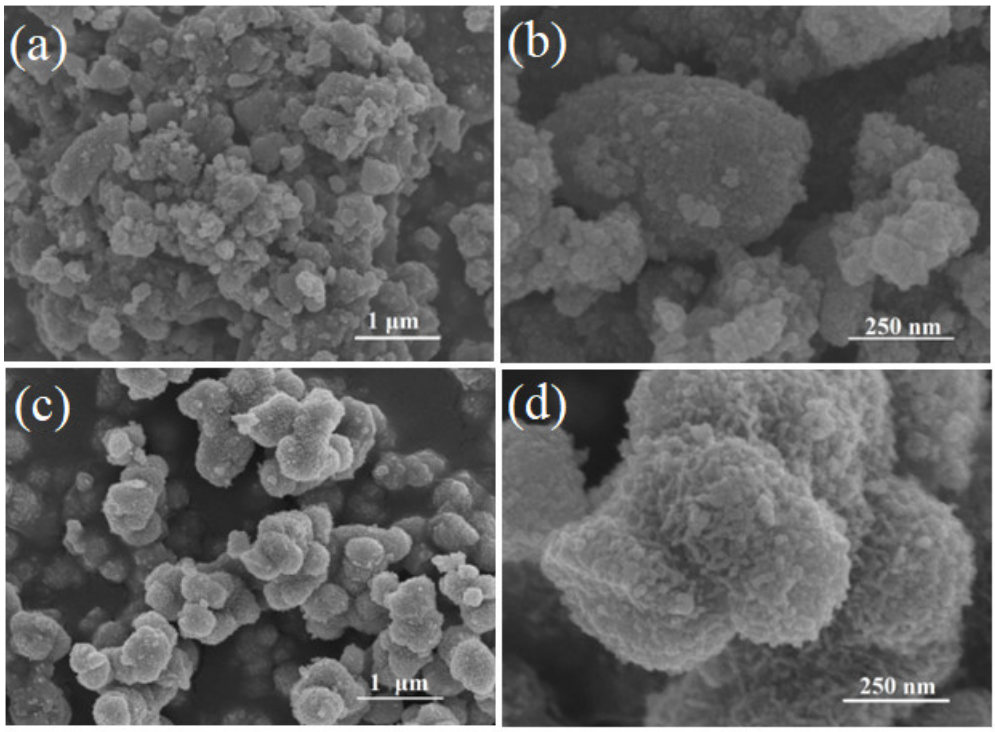

Figure 3. SEM images of MnO_2-M (**a**,**b**) and MnO_2 (**c**,**d**).

2.1.4. H_2-TPR Analysis

It is well known that the redox property of catalysts is a critical factor for the NH_3-SCR reaction [27]. Therefore, we investigated the reduction behavior of the catalysts by H_2-TPR test, and the results are presented in Figure 4. For the two catalysts, there are two obvious reduction peaks located in the temperature range of 213–400 °C (I) and 400–533 °C (II), which can be assigned to the successive reduction of $MnO_2 \rightarrow Mn_2O_3/Mn_3O_4 \rightarrow MnO$ [28,29]. It should be noted that the reduction of MnO_2-M catalyst starts at a lower temperature but ends up at a higher temperature. In contrast, the two reduction peaks of the MnO_2 catalyst overlap, and the peaks are more concentrated. This difference between the two catalysts may be attributed to their different particle size distributions. Smaller particles in MnO_2-M catalyst are easier to be reduced at a low temperature, while larger particles are more difficult to be reduced because of limited mass transfer. Therefore, the two reduction peaks of the MnO_2-M catalyst have a larger temperature gap due to the varying particle size. By contrast, the uniform particle size in the MnO_2 catalyst leads to a narrow reduction peak. This result indicates that the ball-milling process can create small particles and improve the reduction potentials at low temperature. Furthermore, quantitative analysis data of H_2-TPR are listed in Table 2. Although the two catalysts in the H_2-TPR experiments are reduced to green MnO, the experimental H_2 consumption of the catalysts is significantly less than the theoretical consumption (11.5 mmol/g). This may be due to some manganese in the Mn^{3+} oxidation state in catalysts. In addition, the MnO_2-M

catalyst shows more H_2 consumption than the MnO_2 catalyst, which indicates that there exists more of an Mn^{4+} oxidation state than MnO_2. It has been widely reported that Mn^{4+} is the most effective oxidation state for NO_x conversion [30]. Therefore, the MnO_2-M catalyst can be a significant advantage in NH_3-SCR compared with MnO_2.

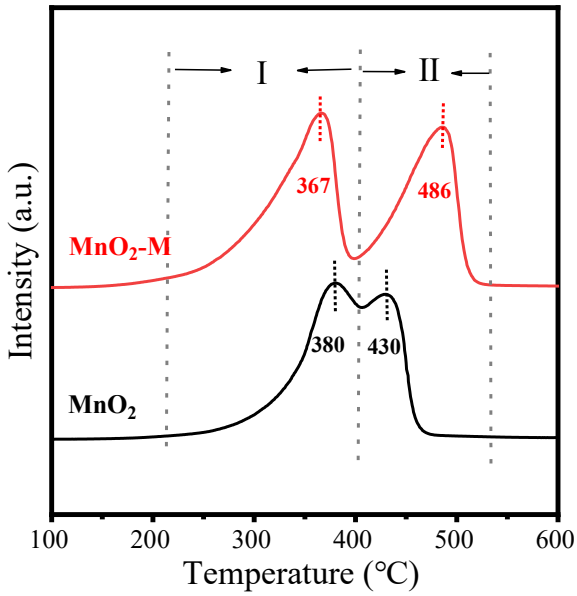

Figure 4. H_2-TPR curves of the catalysts.

Table 2. H_2 adsorption amount of the catalysts.

Catalyst	H_2 Consumption [i] (mmol g^{-1})		Total H_2 Consumption [i] (mmol g^{-1})	Theoretical H_2 Consumption [i] (mmol g^{-1})
	I	II		
MnO_2-M	4.85	3.91	8.76	11.50
MnO_2	3.91	2.27	6.18	11.50

[i] Calculated based on the H_2-TPR results.

2.1.5. XPS Analysis

Figure 5 shows the XPS Mn 2p and O 1s spectra of MnO_2-M and MnO_2 catalysts. The Mn $2p_{3/2}$ spectra can be separated into three characteristic peaks attributed to Mn^{2+} (641.0 eV), Mn^{3+} (642. 4 eV), and Mn^{4+} (643.5 eV), respectively (Figure 5a), by performing peak-fitting deconvolutions [31–34]. The $Mn^{4+}/(Mn^{3+} + Mn^{2+})$ atomic ratio (Table 3) was calculated from XPS spectra. The relative surface content of $Mn^{4+}/(Mn^{3+} + Mn^{2+})$ on MnO_2-M (0.81) is much higher than that of MnO_2 (0.56). Therefore, much more Mn^{4+} is exposed on the surface of the MnO_2-M catalyst, which is beneficial for NO oxidation to NO_2, leading to high activity in the NH_3-SCR reaction at low temperatures.

Two peaks can be distinguished in the O 1s spectra of the catalysts (Figure 5b). The peak at 529.9 eV is assigned to the lattice oxygen (marked as O_{latt}), and the peak at 531.3 eV is ascribed to the surface adsorbed oxygen (marked as O_{ads}, O_2^{2-} or O^- belonging to defect-oxide or hydroxyl-like group) [35,36]. It is well known that the O_{ads} species are more active than the O_{latt} species due to their higher mobility [37]. From Table 3, the O_{ads}/O_{latt} ratio in MnO_2-M (1.17) is much higher than that in MnO_2 (0.60), suggesting that the ball-milling process could produce much more OVs in the MnO_2-M catalyst. The above results show that the MnO_2-M catalyst has a higher $Mn^{4+}/(Mn^{3+} + Mn^{2+})$ content and more surface oxygen species than the MnO_2 catalyst, which is critical to the NH_3-SCR reaction.

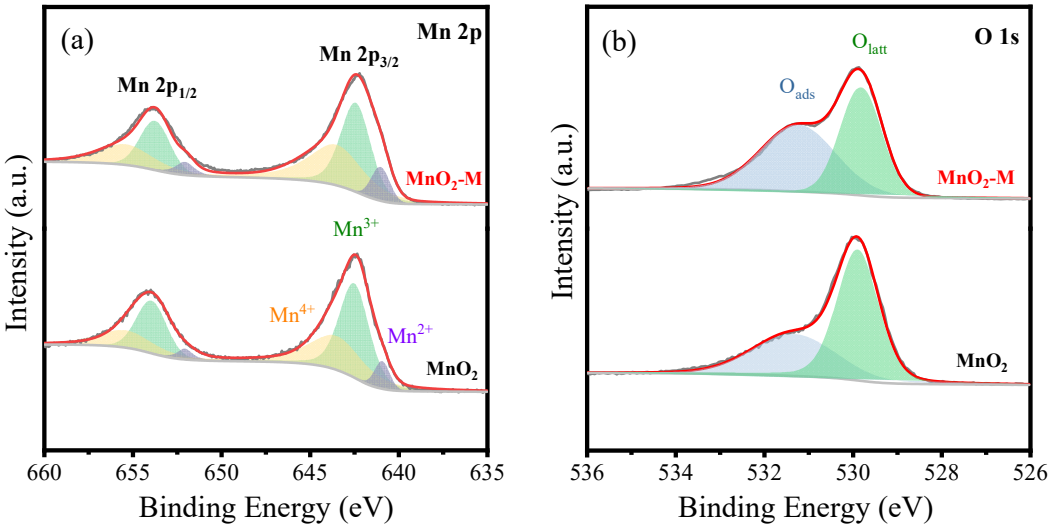

Figure 5. XPS spectra: Mn 2p (**a**) and O 1s (**b**) of the catalysts.

Table 3. Surface compositions of the catalysts by XPS analysis.

Catalyst	$Mn^{4+}/(Mn^{3+} + Mn^{2+})$	O_{ads}/O_{latt}
MnO_2-M	0.81	1.17
MnO_2	0.56	0.60

2.1.6. NH_3-TPD Analysis

The surface acidity of the catalyst also plays a vital role in the low-temperature SCR of NO by NH_3. Therefore, NH_3-TPD was carried out to evaluate the acidity of the catalysts, as shown in Figure 6. The detailed ammonia desorption parameters of the catalysts are summarized in Table 4. From Figure 6, both MnO_2-M and MnO_2 catalysts exhibit one broad desorption peak below 300 °C, which can be attributed to the subsequent desorption of NH_3 coordinated with weak acid sites [36]. As shown in Table 4, the total amount of desorbed NH_3 for MnO_2-M (0.43 μmol g^{-1}) is higher than that of MnO_2 (0.32 μmol g^{-1}), possibly due to the larger specific surface area of the MnO_2-M catalyst. The superiority of acid sites on the MnO_2-M catalyst could promote the adsorption and activation of NH_3, which favors the SCR reaction [38].

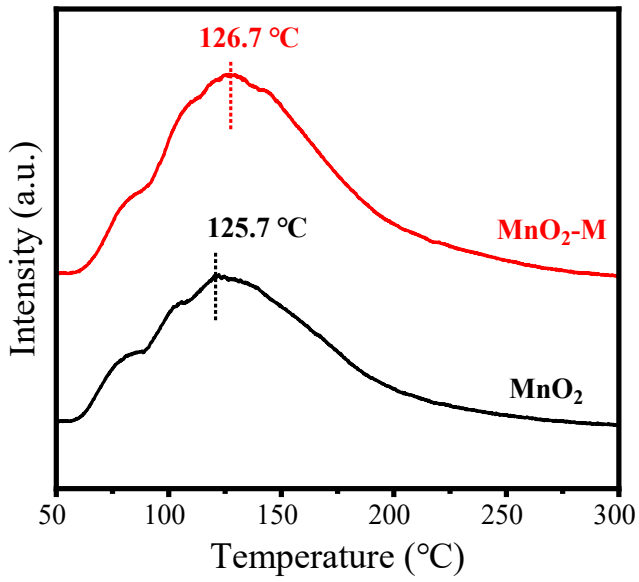

Figure 6. NH_3-TPD curves of the catalysts.

Table 4. Quantitative analysis of NH_3-TPD over the catalysts.

Catalyst	Surface Acidity [i] (μmol g^{-1})
MnO_2-M	0.43
MnO_2	0.32

[i] Calculated based on the NH_3-TPD results.

2.2. Formation Mechanism of MnO_2-M

Previously, studies reported that MnO_2 with different morphology structures could be obtained by tailoring manganese precursors, such as $MnCl_2$, $MnSO_4 \cdot H_2O$, $Mn(NO_3)_2$ H_2O, and $KMnO_4$ [39]. Here, we used $Mn(NO_3)_2$ solution and $KMnO_4$ as precursors. Mn precursors underwent an oxidation-reduction reaction ($2KMnO_4 + 3Mn(NO_3)_2 + 2H_2O = 5MnO_2 + HNO_3 + 2KNO_3$) to generate MnO_2 sediment (Scheme 1). Ball-milling as a mechanical technique is widely used to grind powders into fine particles. When ball-milling was introduced into the catalyst preparation process, these Mn^{2+} and Mn^{7+} precursors could quickly react and convert to irregular MnO_2-M particles with uneven particle size. The crystal cannot grow due to inadequate time, evidenced by SEM and PSD results. The irregular particles with variable sizes in MnO_2-M benefit the formation of inter-particle pores, thereby increasing the surface area of the catalyst. The higher the surface area, the more active sites are available for NH_3-SCR reaction. Considering the ball milling method is an environmentally friendly and cost-effective technique, the facile ball milling-assisted synthesized strategy provides the potential for the scaled-up production of MnO_x catalysts in industrial applications.

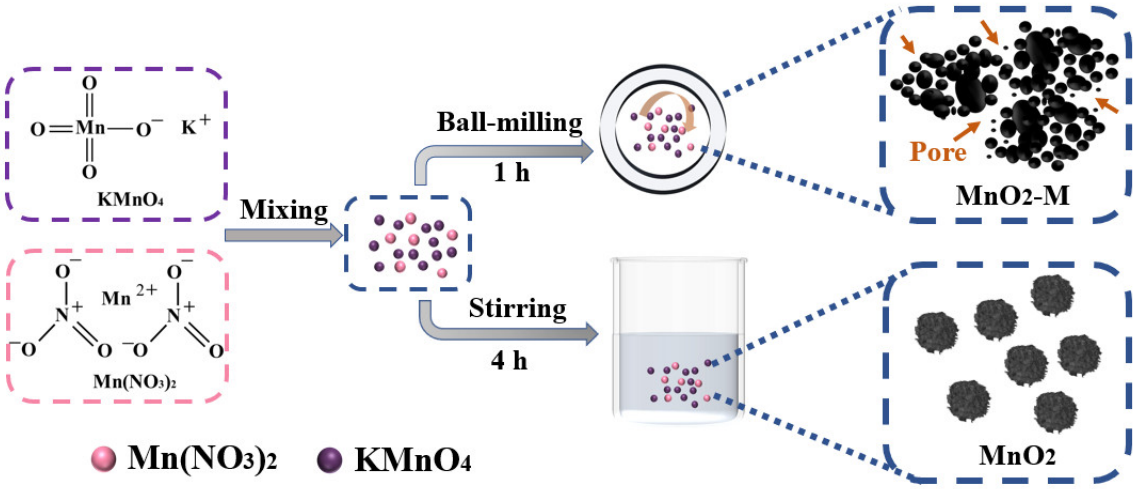

Scheme 1. Schematic illustration of the preparation of catalysts.

2.3. Catalytic Performance

Figure 7a shows the NO_x conversion as a function of temperature in the NH_3-SCR reaction on MnO_2-M and MnO_2 catalysts. MnO_2-M exhibits higher activity with NO_x conversion of 68% at 50 °C and 100% at 100 °C. In contrast, only 49.8% NO_x conversion is obtained at 50 °C on MnO_2, and 100% NO_x conversion is not achieved even at 200 °C. In addition, the N_2 selectivity of the catalysts was evaluated, and the results are shown in Figure 7b. Both the catalysts exhibit an acceptable and similar N_2 selectivity below 150 °C.

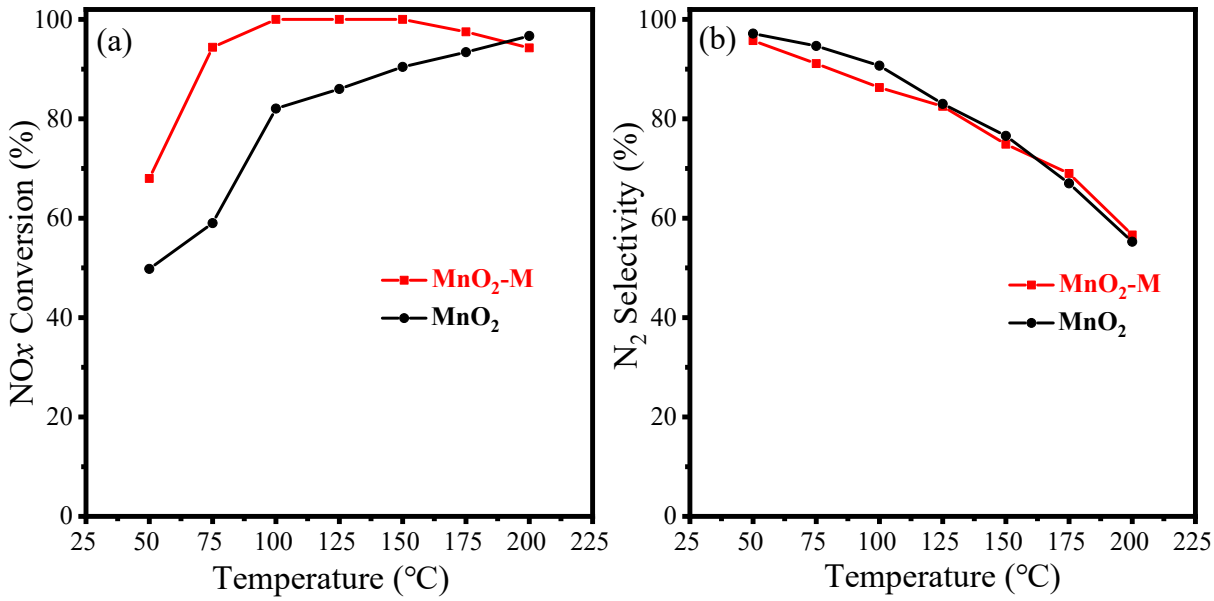

Figure 7. Catalytic performances of the catalysts NO_x conversion (**a**) and N_2 selectivity (**b**) at different temperature (reaction conditions: [NO] = 500 ppm, [NH_3] = 500 ppm, [O_2] = 5%, and N_2 as balance gas, GHSV = 40,000 h^{-1}).

Based on the results of BET, H_2-TPR, XPS, and NH_3-TPD, the much higher NO_x conversion on MnO_2-M can be attributed to its higher specific surface area, more adsorbed surface oxygen, higher reducibility, and more acid sites. It should be noted that the preparation process of the two catalysts is similar, except that the latter uses ball milling. Therefore, it can be deduced that the ball-milling process may be the key to the optimization of catalyst structure and the improvement in the SCR performance. To verify this, we applied the ball milling method to the MnO_2 catalyst and obtained the M-MnO_2 catalyst. As shown in Figure 8, the M-MnO_2 catalyst presents an NO_x conversion of 55% at 50 °C, 78% at 75 °C, and 97% at 100 °C, suggesting a much better NH_3-SCR performance than the pristine MnO_2.

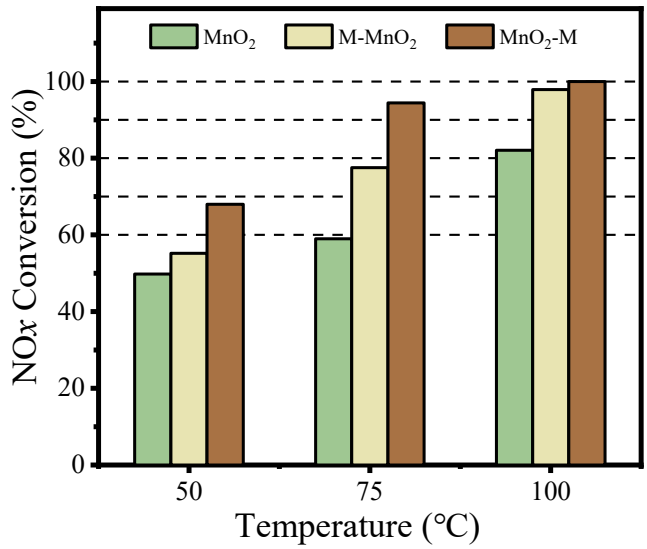

Figure 8. Comparison of NO_x conversion of MnO_2, MnO_2-M, and M-MnO_2 catalysts at different temperature (reaction conditions: [NO] = 500 ppm, [NH_3] = 500 ppm, [O_2] = 5%, and N_2 as balance gas, GHSV = 40,000 h^{-1}).

The resistance to H_2O and SO_2 under reaction conditions is important for low-temperature SCR catalysts. The H_2O and SO_2 tolerance tests of the MnO_2-M and MnO_2 were conducted at 150 °C. Figure 9a shows the H_2O tolerance results of the catalysts. When 10 vol.% H_2O is added to the reaction gas, the NO_x conversion on the MnO_2-M catalyst changes from nearly 100% at 4 h to 85.5% at 14 h, and that of MnO_2 decreases from nearly 100% at 4 h to 76.9% at 14 h, suggesting that the MnO_2-M catalyst shows better resistance to H_2O than MnO_2. When H_2O is cut off, its catalytic activities recover quickly. In particular, the MnO_2-M catalyst can be fully recovered to the original level. Therefore, the activity decreases in the two catalysts caused by H_2O originated from competitive adsorption of H_2O and NH_3/NO_x for active sites, but not the deactivation of active sites. As shown in Figure 9b, further introduction of SO_2 to the reaction gas significantly decreased the initial NO_x conversion over the two catalysts compared to the case of only H_2O. In addition, the NO_x conversions of the two catalysts decrease gradually along with reaction time. However, the NO_x conversion on the MnO_2-M catalyst is still much higher than that on MnO_2. Moreover, when the H_2O and SO_2 are removed from the reaction gas, the NO_x conversions of the MnO_2-M and MnO_2 catalysts cannot recover, which may be due to the formation of sulfating Mn species. Even so, the MnO_2-M catalyst could achieve more than 88.4% NO_x conversion after the process, implying that it has good resistance to H_2O and SO_2.

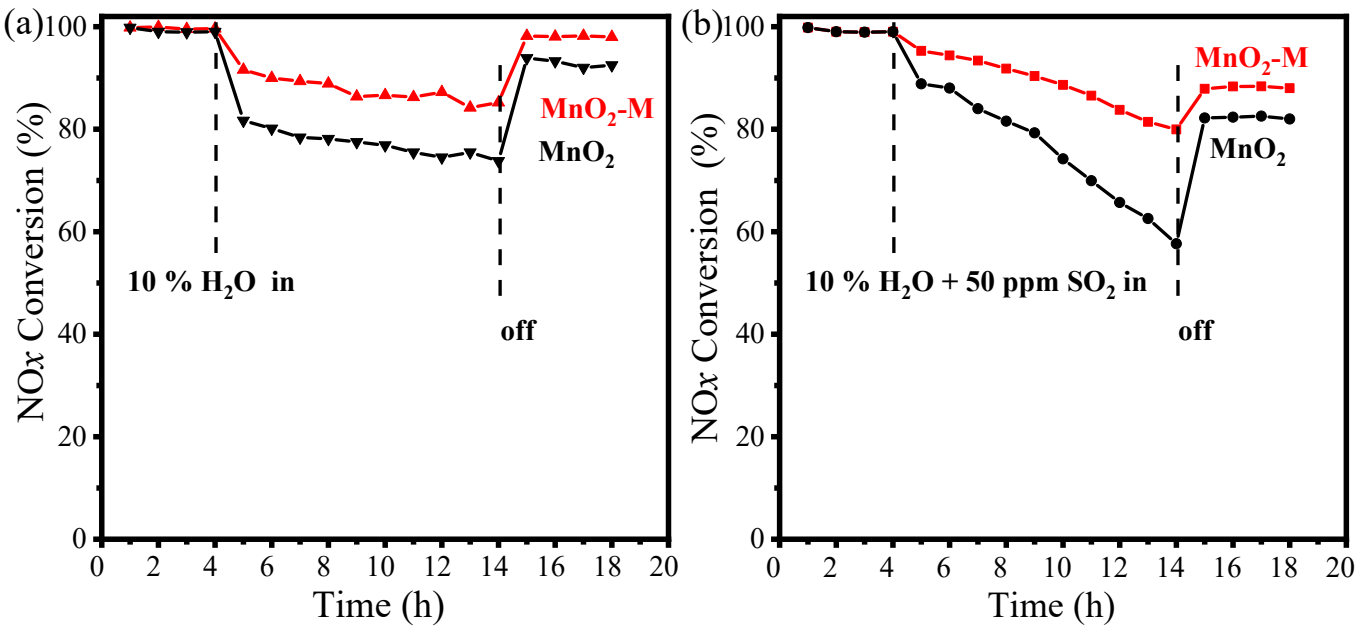

Figure 9. The effect of H_2O on NO_x conversion over the catalysts (**a**) and the effect of SO_2 and H_2O on NO_x conversion at 150 °C (**b**) (reaction conditions: [NO] = 500 ppm, [NH_3] = 500 ppm, [O_2] = 5%, and N_2 as balance gas, [H_2O(g)] = 10 vol.% (in use), [SO_2] = 50 ppm (in use), GHSV = 40,000 h^{-1}).

2.4. In Situ DRIFTS Studies

To obtain insights about the reaction mechanism, in situ DRIFTS studies were conducted. In situ DRIFTS spectra of MnO_2-M and MnO_2 catalysts exposed to NO + O_2 at 50 °C as a function of time are shown in Figure 10. Four main bands over the two catalysts appear after introducing NO + O_2 into the IR cell. For the MnO_2-M catalyst, the band located at 1026 cm^{-1} is ascribed to monodentate nitrite, while those at 1539 and 1271 cm^{-1} are assigned to bidentate nitrate. The band at 1630 cm^{-1} is attributed to the NO_2 ad-species (nitro group or adsorbed NO_2 molecule) [40,41]. The intensity of these peaks becomes stronger with the increase in exposure time. On the MnO_2 catalyst, the bands assigned to monodentate nitrite and the NO_2 ad-species at 1031 and 1620 cm^{-1} are also detected. Additionally, the bands that are indexed to monodentate nitrates (1313 cm^{-1}) and ionic

nitrate (1462 cm^{-1}) appear on the MnO_2 catalyst. However, those bands corresponding to bidentate nitrate disappear. The above results show that more stable nitrate exists, e.g., the bidentate nitrate on the MnO_2-M catalyst, which further proves that the formation of more OVs on the MnO_2-M catalyst promotes NH_3-SCR performance.

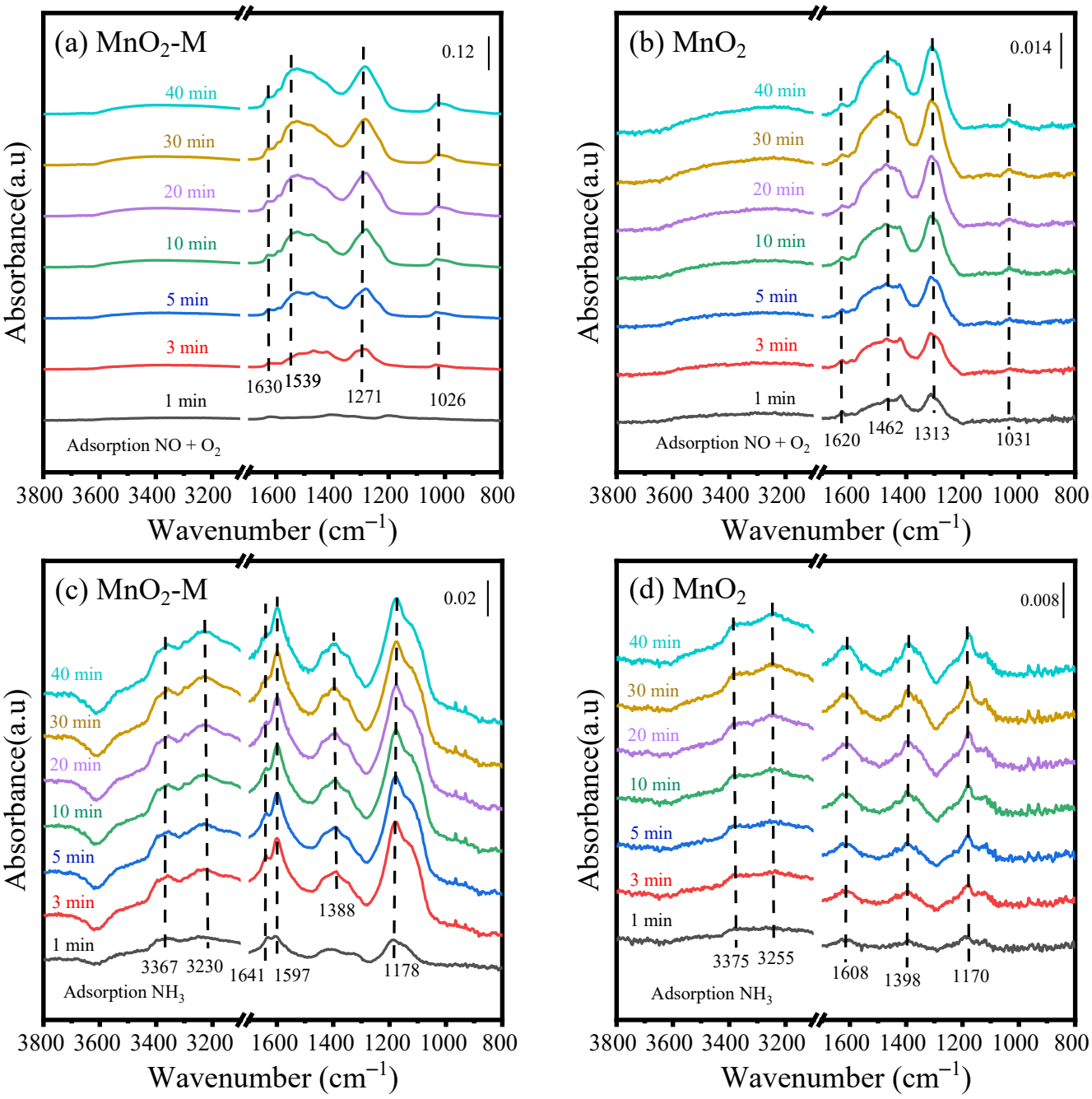

Figure 10. In situ DRIFTS spectra of adsorption of NO + O_2 at 50 °C on MnO_2-M (**a**) and MnO_2 (**b**). In situ DRIFTS spectra of NH_3 adsorption at 50 °C on MnO_2-M (**c**) and MnO_2 (**d**).

To investigate the nature of the adsorbed NH_3 species and potential intermediates, in situ DRIFTS spectra of the two catalysts exposed in the NH_3 atmosphere at 50 °C were collected, as shown in Figure 10c,d. The bands in 3450–3000 cm^{-1} can be assigned to N-H stretching vibration of ordinated NH_3 adsorbed on Lewis sites [42,43]. The corresponding bending vibrations are observed at 1170/1178 cm^{-1} [42–44]. With the increasing adsorption time, the bands of the two catalysts increase until the adsorption is saturated. For the MnO_2-

M catalyst, the band at 1597 cm^{-1} is assigned to NH_3 coordinately linked to the Lewis acid sites, while the band at 1388 cm^{-1} can be ascribed to monodentate nitrites. In Figure 10d, these bands show a little shift over the MnO_2 catalyst, e.g., from 1597 cm^{-1} and 1388 cm^{-1} to 1608 cm^{-1} and 1398 cm^{-1}, respectively. Compared with the MnO_2 catalyst, a new band at 1641 cm^{-1} corresponding to bridging nitrates appears. This indicates that partial NH_3 at Lewis acid sites can be oxidized to bidentate nitrate and monodentate nitrites. The MnO_2-M catalyst possesses stronger acid intensity to absorb the ammonia species, further explaining the higher SCR activity of the MnO_2-M catalyst.

To further investigate the SCR reaction mechanism over the two catalysts, in situ DRIFTS spectra in a flow of NO + O_2 + NH_3 were conducted at different temperatures. As shown in Figure 11, raising the temperature decreased the intensity of all the bands. For the MnO_2-M catalyst at 50 °C, the band at 1196 cm^{-1} is attributed to N-H bending vibrations of NH_3 adsorbed on Lewis sites. The bands at 1319, 1602, and 3200–3400 cm^{-1} are attributed to ordinated NH_3 adsorbed on Lewis sites. And the band at 1319 cm^{-1} shifts to lower wavenumbers with the increasing temperature, eventually reaching 1278 cm^{-1} at 300 °C. The bands at 1394 cm^{-1} were attributed to monodentate nitrate [40,45]. In situ DRIFTS spectra of the MnO_2 catalyst, as shown in Figure 11c, are similar to those obtained over the MnO_2-M catalyst. However, the intensities of the bands on MnO_2 are much lower than that on the MnO_2-M catalyst, possibly due to the less active sites in the MnO_2 catalyst.

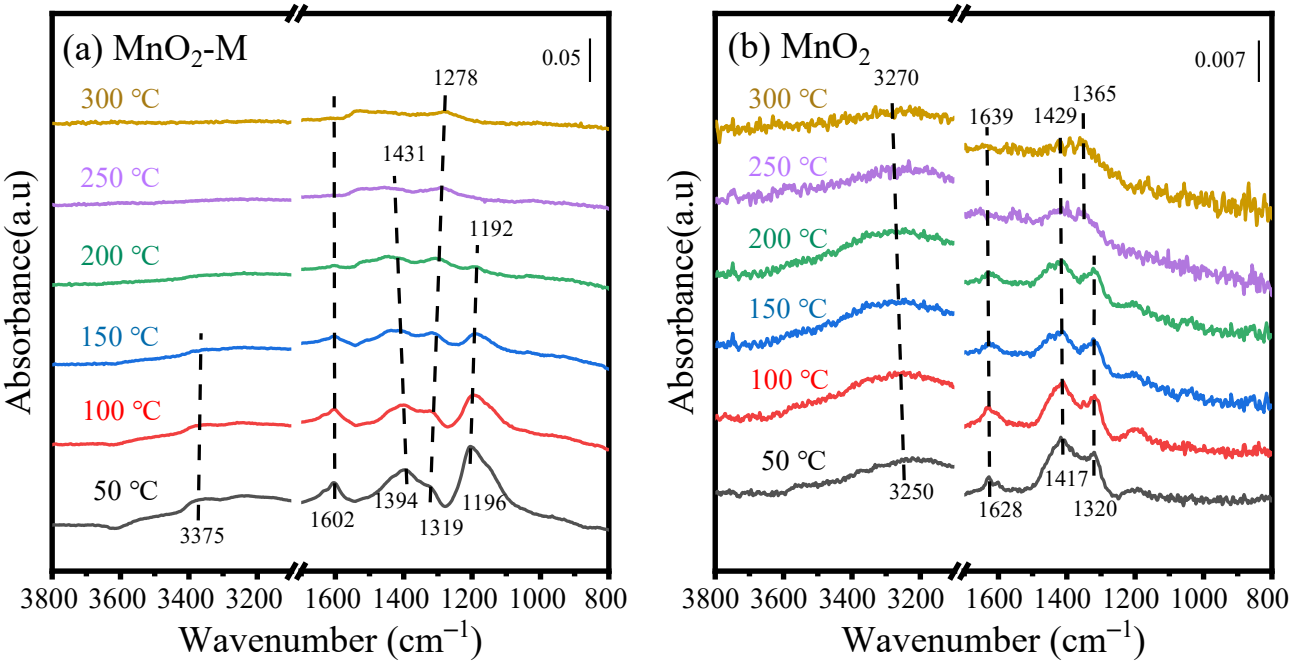

Figure 11. In situ DRIFTS spectra of adsorption of NO + O_2 + NH_3 at a different temperature over MnO_2-M (**a**) and MnO_2 (**b**).

The above results suggest that the adsorption of NH_3 is dominated under the SCR reaction conditions for the two catalysts. The possible reaction mechanism over MnO_2-M at low temperature can be described in Scheme 2. The NO molecules in the gas phase are adsorbed on the catalyst surface and react with O_2 with OVs' assistance to form NO_2. Due to Lewis acidity, the NH_3 molecules are adsorbed onto the MnO_2-M surface and form NH_3(ad). Then, the formed NH_3(ad) can further react with NO_x to generate N_2 and H_2O. Therefore, the SCR reaction on MnO_2-M proceeds via the typical Eley–Rideal (ER) mechanism.

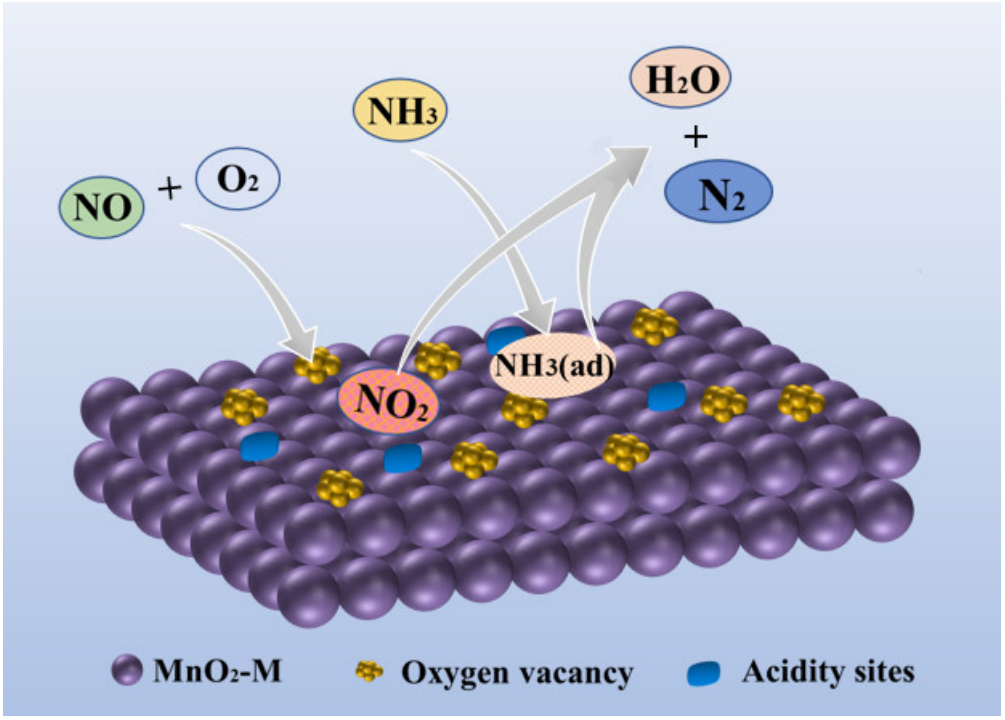

Scheme 2. The main reaction mechanism of the NH_3-SCR over the MnO_2-M catalyst.

3. Experiment

3.1. Chemical Reagents

Manganese nitrate solution ($Mn(NO_3)_2$, 50% in H_2O) was purchased from Shanghai Macklin Biochemical Co., Ltd., Shanghai, China and potassium permanganate ($KMnO_4$) was purchased from Beijing Chemical Works Co., Ltd., Beijing, China. All the chemicals were analytical grade and used as received without further treatment. Deionized water was used in all experiments.

3.2. Preparation of Catalysts

The Mn-based catalyst was prepared by the ball milling-assisted redox method. Scheme 3 depicts the synthesis procedure of the catalyst. In brief, 3.64 g of $KMnO_4$ and 6.17 g of $Mn(NO_3)_2$ were added to an agate jar (100 mL) along with some zirconia balls (5 mm diameter). Here, the ball to powder mass ratio was 10:1. The agate jar was placed in a high-speed ball milling apparatus (Planetary Ball Mill QM-3SP04, Nanjing Chishun Sclence And Technology Development Co., Ltd, Nanjing, China), and the reactants were ball-milling for 1 h at a frequency of 580 r/min. The resulting solid was washed several times with deionized water, dried overnight at 105 °C, and calcined at 400 °C for 3 h to obtain the Mn-based catalyst. The prepared catalyst was denoted as MnO_2-M.

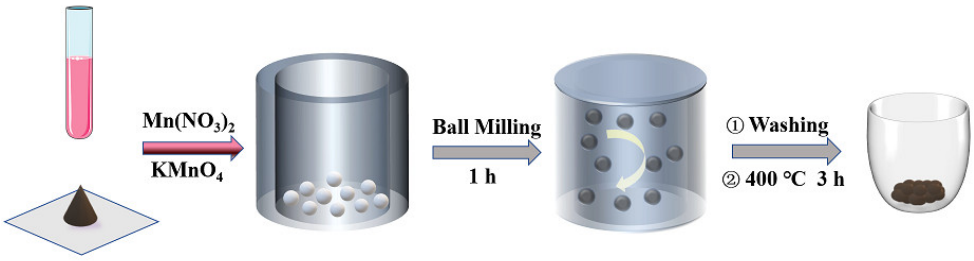

Scheme 3. Synthesis procedures for the preparation of the MnO_2-M catalyst.

For comparison, the MnO_2 catalyst was prepared without ball milling. First, 3.64 g of $KMnO_4$ was dissolved in 100 mL of deionized water to obtain solution A. Next, 6.17 g of

$Mn(NO_3)_2$ was dissolved in 100 mL of deionized water to obtain solution B. Subsequently, solution B was added dropwise into solution A under stirring at room temperature, and the obtained mixture was stirred for 4 h to form a slurry. Then, the slurry was filtered and washed several times with deionized water. The filter cake was dried overnight at 105 °C and calcined at 400 °C for 3 h. The obtained catalyst was named MnO_2. For comparison with MnO_2 and MnO_2-M, part of the synthesized MnO_2 catalyst was further ball-milled for 1 h, obtaining the reference catalyst named M-MnO_2.

3.3. Characterization

X-ray diffraction (XRD) patterns were recorded using a Cu Kα radiation (λ = 1.5148 Å) range from 10.0 to 90.0° (X'Pert PRO MPD, PANalytical, Almelo, the Netherlands). The scanning electron micrograph (SEM) images were obtained at 5.0 kV (Regulus 8100, JEOL, Tokyo, Japan). The particle size distribution (PSD) was measured using a laser particle size analyzer (BT-9300Z, Bettersize Instruments Ltd., Dandong, China). The N_2 adsorption-desorption isotherms were measured on a surface area and pore size analyzer (NOVA 3200e, Quantachrome, FL, USA). The specific surface areas of the catalysts were determined by using the Brunauer–Emmett–Teller (BET) method. The catalysts were degassed at 200 °C for 4 h and analyzed at −196 °C. The pore volume and pore size distribution were measured from the desorption branch using the Barrett–Joyner–Halenda (BJH) method.

H_2 temperature-programmed reduction (H_2-TPR) experiments were carried out on an automated chemisorption analyzer (ChemBET pulsar TPR/TPD, Quantachrome, FL, USA). 0.05 g of catalyst was loaded into a quartz U-tube, then the catalyst was degassed at 150 °C for 0.5 h under helium. When the temperature was cooled to 50 °C, the gas was changed to 10% H_2/Ar. Finally, the catalyst was heated from 50 to 1000 °C at 10 °C min^{-1} under a H_2/Ar flow (30 mL min^{-1}). X-ray photoelectron spectra (XPS) were collected to analyze the surface chemical compositions of the catalysts (Model VG ESCALAB 250 spectrometer, Thermo Electron, London, UK). Temperature-programmed desorption of ammonia (NH_3-TPD) experiments were carried out on a FT-IR instrument (Nicolet 380, Thermo Fisher Scientific, Waltham, MA, USA). Before the experiment, 100 mg of catalyst was treated in 5% O_2/N_2 at 300 °C for 30 min. After cooling to 50 °C in the same gas mixture, the catalyst was exposed to 500 ppm NH_3/N_2 for 30 min and then flushed in N_2 gas flow for 30 min. The NH_3 desorption was recorded in N_2 while heating to 500 °C at a rate of 10 °C/min. In situ diffuse reflectance infrared Fourier transform spectroscopy (in situ DRIFTS) of the catalyst was carried out with an FTIR (Nicolet iS50, Thermo Fisher Scientific, Waltham, MA, USA) equipped with an in situ diffuse reflection chamber and MCT detector. The catalysts were pretreated at 300 °C in a 5% O_2/N_2 atmosphere for 30 min and then gradually cooled to 50 °C. Then, the catalysts were purged with the reaction atmosphere, and the spectra were collected as a function of time.

3.4. Catalytic Measurement

The NH_3-SCR activity reaction was carried out in a fixed-bed reactor operating at atmospheric pressure. Before each test, 1.5 mL of catalyst was pretreated with N_2 gas flow in the reactor at 300 °C for 1 h. The inlet gas comprised NO (500 ppm), NH_3 (500 ppm), O_2 (5%), and N_2 (the balance). The GHSV was 40,000 h^{-1}. A FT-IR spectrometer monitored the gaseous species (NO, NH_3, NO_2, and N_2O) in the exhaust (Nicolet 380, Thermo Fisher Scientific, Waltham, MA, USA).

The NH_3-SCR stability reaction was carried out in a fixed-bed reactor operating at atmospheric pressure. Before each test, 1.5 mL of catalyst was pretreated with N_2 gas flow in the reactor at 300 °C for 1 h. The inlet gas comprised NO (500 ppm), NH_3 (500 ppm), O_2 (5%), SO_2 (50 ppm, in use), H_2O (10 vol.%, in use), and N_2 (the balance). The GHSV was 40,000 h^{-1}. The NO_x concentrations in the exhaust were analyzed by a multiple gas

analyzer (Testo 350, Testo SE & Co. KGaA, Baden-Württemberg, Germany). The NO_x conversion and N_2 selectivity were calculated as follows:

$$NO_x \text{ conversion } (\%) = \frac{[NO_x]_{in} - [NO_x]_{out} - 2 \times [N_2O]_{out}}{[NO_x]_{in}} \times 100 \quad (1)$$

$$N_2 \text{ selectivity } (\%) = (1 - \frac{2 \times [N_2O]_{out}}{[NH_3]_{in} - [NH_3]_{out} + [NO_x]_{in} - [NO_x]_{out}}) \times 100 \quad (2)$$

The "in" and "out" subscripts represent the inlet and outlet gas concentrations in the steady state, respectively.

4. Conclusions

The ball milling-assisted redox method was successfully applied to prepare the MnO_2-M catalyst with a high specific surface area. Compared with the MnO_2 catalyst obtained by the redox method, the MnO_2-M catalyst exhibits a higher catalytic activity and better resistance against H_2O and SO_2 in NH_3-SCR reaction at low temperatures. Based on characterization analysis, more OVs can be manufactured, which is beneficial for NO oxidation and promotes the NH_3-SCR reaction. Moreover, the MnO_2-M catalyst has more acid sites, higher Mn^{4+} content, surface adsorbed oxygen, and active sites. All these features can contribute to the high NH_3-SCR performance of the MnO_2-M catalyst. In situ DRIFTS studies probed the reaction intermediates and predicted that the adsorption of NH_3 is dominated under the SCR reaction via the typical Eley–Rideal mechanism.

Author Contributions: Conceptualization, B.J. and F.S.; methodology, Y.D., B.J., S.L. and F.S.; validation, Y.D.; formal analysis, Y.D.; investigation, Y.D.; resources, K.W.; data curation, Y.D. and S.L.; writing—original draft preparation, Y.D.; writing—review and editing, B.J., J.G. and F.S.; visualization, Y.D., B.J. and F.S.; supervision, B.J. and F.S.; project administration, F.S.; funding acquisition, F.S. All authors have read and agreed to the published version of the manuscript.

Funding: This research received no external funding.

Data Availability Statement: The data presented in this study are available on request from the corresponding author.

Acknowledgments: We gratefully acknowledge the financial support from the Beijing Chenxi Environmental Engineering Co., Ltd.

Conflicts of Interest: The authors declare no conflict of interest.

References

1. Liu, Z.; Liu, Y.; Li, Y.; Su, H.; Ma, L. WO_3 promoted Mn–Zr mixed oxide catalyst for the selective catalytic reduction of NO_x with NH_3. *Chem. Eng. J.* **2016**, *283*, 1044–1050. [CrossRef]
2. Anenberg, S.C.; Miller, J.; Minjares, R.; Du, L.; Henze, D.K.; Lacey, F.; Malley, C.S.; Emberson, L.; Franco, V.; Klimont, Z.; et al. Impacts and mitigation of excess diesel-related NO_x emissions in 11 major vehicle markets. *Nature* **2017**, *545*, 467–471. [CrossRef] [PubMed]
3. Xie, S.; Tan, W.; Li, Y.; Ma, L.; Ehrlich, S.N.; Deng, J.; Xu, P.; Gao, F.; Dong, L.; Liu, F. Copper Single Atom-Triggered Niobia–Ceria Catalyst for Efficient Low-Temperature Reduction of Nitrogen Oxides. *ACS Catal.* **2022**, *12*, 2441–2453. [CrossRef]
4. Yao, X.; Zhang, L.; Li, L.; Liu, L.; Cao, Y.; Dong, X.; Gao, F.; Deng, Y.; Tang, C.; Chen, Z.; et al. Investigation of the structure, acidity, and catalytic performance of $CuO/Ti_{0.95}Ce_{0.05}O_2$ catalyst for the selective catalytic reduction of NO by NH_3 at low temperature. *Appl. Catal. B Environ.* **2014**, *150–151*, 315–329. [CrossRef]
5. Forzatti, P.; Nova, I.; Tronconi, E. Enhanced NH_3 Selective Catalytic Reduction for NO_x Abatement. *Angew. Chem.* **2009**, *121*, 8516–8518. [CrossRef]
6. Xu, L.; Wang, C.; Chang, H.; Wu, Q.; Zhang, T.; Li, J. New Insight into SO_2 Poisoning and Regeneration of CeO_2-WO_3/TiO_2 and V_2O_5-WO_3/TiO_2 Catalysts for Low-Temperature NH_3-SCR. *Environ. Sci. Technol.* **2018**, *52*, 7064–7071. [CrossRef]
7. Qiu, Y.; Liu, B.; Du, J.; Tang, Q.; Liu, Z.; Liu, R.; Tao, C. The monolithic cordierite supported V_2O_5–MoO_3/TiO_2 catalyst for NH_3-SCR. *Chem. Eng. J.* **2016**, *294*, 264–272. [CrossRef]
8. Chen, H.; Xia, Y.; Fang, R.; Huang, H.; Gan, Y.; Liang, C.; Zhang, J.; Zhang, W.; Liu, X. The effects of tungsten and hydrothermal aging in promoting NH_3-SCR activity on V_2O_5/WO_3-TiO_2 catalysts. *Appl. Surf. Sci.* **2018**, *459*, 639–646. [CrossRef]

9. Beretta, A.; Lanza, A.; Lietti, L.; Alcove Clave, S.; Collier, J.; Nash, M. An investigation on the redox kinetics of NH_3-SCR over a V/Mo/Ti catalyst: Evidence of a direct role of NO in the re-oxidation step. *Chem. Eng. J.* **2019**, *359*, 88–98. [CrossRef]
10. Liu, L.; Xu, K.; Su, S.; He, L.; Qing, M.; Chi, H.; Liu, T.; Hu, S.; Wang, Y.; Xiang, J. Efficient Sm modified Mn/TiO_2 catalysts for selective catalytic reduction of NO with NH_3 at low temperature. *Appl. Catal. A Gen.* **2020**, *592*, 117413. [CrossRef]
11. Zhang, N.; Yan, H.; Li, L.; Wu, R.; Song, L.; Zhang, G.; Liang, W.; He, H. Use of rare earth elements in single-atom site catalysis: A critical review—Commemorating the 100th anniversary of the birth of Academician Guangxian Xu. *J. Rare Earths* **2021**, *39*, 233–242. [CrossRef]
12. Jia, L.; Liu, J.; Huang, D.; Zhao, J.; Zhang, J.; Li, K.; Li, Z.; Zhu, W.; Zhao, Z.; Liu, J. Interface Engineering of a Bifunctional Cu-SSZ-13@CZO Core–Shell Catalyst for Boosting Potassium Ion and SO_2 Tolerance. *ACS Catal.* **2022**, *12*, 11281–11293. [CrossRef]
13. Chen, L.; Li, R.; Li, Z.; Yuan, F.; Niu, X.; Zhu, Y. Effect of Ni doping in $Ni_xMn_{1-x}Ti_{10}$ (x = 0.1–0.5) on activity and SO_2 resistance for NH_3-SCR of NO studied with in situ DRIFTS. *Catal. Sci. Technol.* **2017**, *7*, 3243–3257. [CrossRef]
14. Raja, S.; Alphin, M.S.; Sivachandiran, L.; Singh, P.; Damma, D.; Smirniotis, P.G. TiO_2-carbon nanotubes composite supported MnO_x-CuO catalyst for low-temperature NH_3-SCR of NO: Investigation of SO_2 and H_2O tolerance. *Fuel* **2022**, *307*, 121886. [CrossRef]
15. Yang, J.; Ren, S.; Zhou, Y.; Su, Z.; Yao, L.; Cao, J.; Jiang, L.; Hu, G.; Kong, M.; Yang, J.; et al. In situ IR comparative study on N_2O formation pathways over different valence states manganese oxides catalysts during NH_3–SCR of NO. *Chem. Eng. J.* **2020**, *397*, 125446. [CrossRef]
16. Tang, X.; Hao, J.; Xu, W.; Li, J. Low temperature selective catalytic reduction of NO with NH_3 over amorphous MnO_x catalysts prepared by three methods. *Catal. Commun.* **2007**, *8*, 329–334. [CrossRef]
17. Fang, X.; Liu, Y.; Cen, W.; Cheng, Y. Birnessite as a Highly Efficient Catalyst for Low-Temperature NH_3-SCR: The Vital Role of Surface Oxygen Vacancies. *Ind. Eng. Chem. Res.* **2020**, *59*, 14606–14615. [CrossRef]
18. Liu, J.; Wei, Y.; Li, P.-Z.; Zhang, P.; Su, W.; Sun, Y.; Zou, R.; Zhao, Y. Experimental and Theoretical Investigation of Mesoporous MnO_2 Nanosheets with Oxygen Vacancies for High-Efficiency Catalytic DeNOx. *ACS Catal.* **2018**, *8*, 3865–3874. [CrossRef]
19. Chen, H.; Yang, M.; Tao, S.; Chen, G. Oxygen vacancy enhanced catalytic activity of reduced Co_3O_4 towards p-nitrophenol reduction. *Appl. Catal. B Environ.* **2017**, *209*, 648–656. [CrossRef]
20. Sun, M.; Li, W.; Zhang, B.; Cheng, G.; Lan, B.; Ye, F.; Zheng, Y.; Cheng, X.; Yu, L. Enhanced catalytic performance by oxygen vacancy and active interface originated from facile reduction of OMS-2. *Chem. Eng. J.* **2018**, *331*, 626–635. [CrossRef]
21. Hilpert, K.; Steinbrech, R.W.; Boroomand, F.; Wessel, E.; Meschke, F.; Zuev, A.; Teller, O.; Nickel, H.; Singheiser, L. Defect formation and mechanical stability of perovskites based on $LaCrO_3$ for solid oxide fuel cells (SOFC). *J. Eur. Ceram. Soc.* **2003**, *23*, 3009–3020. [CrossRef]
22. Yim, C.M.; Pang, C.L.; Thornton, G. Oxygen vacancy origin of the surface band-gap state of TiO_2(110). *Phys. Rev. Lett.* **2010**, *104*, 036806. [CrossRef] [PubMed]
23. Wu, S.; Liu, H.; Huang, Z.; Xu, H.; Shen, W. O-vacancy-rich porous MnO_2 nanosheets as highly efficient catalysts for propane catalytic oxidation. *Appl. Catal. B Environ.* **2022**, *312*, 121387. [CrossRef]
24. Ji, J.; Lu, X.; Chen, C.; He, M.; Huang, H. Potassium-modulated δ-MnO_2 as robust catalysts for formaldehyde oxidation at room temperature. *Appl. Catal. B Environ.* **2020**, *260*, 118210. [CrossRef]
25. Chen, L.; Ren, S.; Xing, X.; Yang, J.; Li, J.; Yang, J.; Liu, Q. Effect of MnO_2 crystal types on CeO_2@MnO_2 oxides catalysts for low-temperature NH_3-SCR. *J. Environ. Chem. Eng.* **2022**, *10*, 108239. [CrossRef]
26. Huang, N.; Qu, Z.; Dong, C.; Qin, Y.; Duan, X. Superior performance of α@β-MnO_2 for the toluene oxidation: Active interface and oxygen vacancy. *Appl. Catal. A Gen.* **2018**, *560*, 195–205. [CrossRef]
27. Wang, Y.; Li, Z.; Ding, Z.; Kang, N.; Fan, R.; Wang, Y.; Zhang, C.; Guo, X.; Wang, R. Effect of Ion-Exchange Sequences on Catalytic Performance of Cerium-Modified Cu-SSZ-13 Catalysts for NH_3-SCR. *Catalysts* **2021**, *11*, 997. [CrossRef]
28. Andreoli, S.; Deorsola, F.A.; Pirone, R. MnO_x-CeO_2 catalysts synthesized by solution combustion synthesis for the low-temperature NH_3-SCR. *Catal. Today* **2015**, *253*, 199–206. [CrossRef]
29. Li, S.; Huang, B.; Yu, C. A CeO_2-MnO_x core-shell catalyst for low-temperature NH_3-SCR of NO. *Catal. Commun.* **2017**, *98*, 47–51. [CrossRef]
30. Duan, X.; Dou, J.; Zhao, Y.; Khoshk Rish, S.; Yu, J. A Study on Mn-Fe Catalysts Supported on Coal Fly Ash for Low-Temperature Selective Catalytic Reduction of NO_x in Flue Gas. *Catalysts* **2020**, *10*, 1399. [CrossRef]
31. Chen, C.; Xie, H.; He, P.; Liu, X.; Yang, C.; Wang, N.; Ge, C. Comparison of low-temperature catalytic activity and H_2O/SO_2 resistance of the Ce-Mn/TiO_2 NH_3-SCR catalysts prepared by the reverse co-precipitation, co-precipitation and impregnation method. *Appl. Surf. Sci.* **2022**, *571*, 151285. [CrossRef]
32. Fang, N.; Guo, J.; Shu, S.; Luo, H.; Chu, Y.; Li, J. Enhancement of low-temperature activity and sulfur resistance of $Fe_{0.3}Mn_{0.5}Zr_{0.2}$ catalyst for NO removal by NH_3-SCR. *Chem. Eng. J.* **2017**, *325*, 114–123. [CrossRef]
33. Liu, S.; Ji, Y.; Xu, W.; Zhang, J.; Jiang, R.; Li, L.; Jia, L.; Zhong, Z.; Xu, G.; Zhu, T.; et al. Hierarchically interconnected porous Mn_xCo_{3-x}O4 spinels for Low-temperature catalytic reduction of NO by CO. *J. Catal.* **2022**, *406*, 72–86. [CrossRef]
34. Liu, Y.-z.; Guo, R.-t.; Duan, C.-p.; Wu, G.-l.; Miao, Y.-f.; Gu, J.-w.; Pan, W.-g. A highly effective urchin-like $MnCrO_x$ catalyst for the selective catalytic reduction of NO_x with NH_3. *Fuel* **2020**, *271*, 117667. [CrossRef]

35. Xie, S.; Li, L.; Jin, L.; Wu, Y.; Liu, H.; Qin, Q.; Wei, X.; Liu, J.; Dong, L.; Li, B. Low temperature high activity of M (M = Ce, Fe, Co, Ni) doped M-Mn/TiO_2 catalysts for NH_3-SCR and in situ DRIFTS for investigating the reaction mechanism. *Appl. Surf. Sci.* **2020**, *515*, 146014. [CrossRef]
36. Chen, Z.; Ren, S.; Wang, M.; Yang, J.; Chen, L.; Liu, W.; Liu, Q.; Su, B. Insights into samarium doping effects on catalytic activity and SO_2 tolerance of $MnFeO_x$ catalyst for low-temperature NH_3-SCR reaction. *Fuel* **2022**, *321*, 124113. [CrossRef]
37. Yuan, H.; Sun, N.; Chen, J.; Jin, J.; Wang, H.; Hu, P. Insight into the NH_3-Assisted Selective Catalytic Reduction of NO on β-MnO_2(110): Reaction Mechanism, Activity Descriptor, and Evolution from a Pristine State to a Steady State. *ACS Catal.* **2018**, *8*, 9269–9279. [CrossRef]
38. Meng, Z.; Yan, X.; Cui, M.; Hou, L.; Wu, W. Study on denitration performance of mineral catalyst prepared by high energy ball milling of rare earth concentrate supported Fe_2O_3 for NH_3-SCR. *Mater. Chem. Phys.* **2022**, *276*, 125248. [CrossRef]
39. Xie, Y.; Yu, Y.; Gong, X.; Guo, Y.; Guo, Y.; Wang, Y.; Lu, G. Effect of the crystal plane figure on the catalytic performance of MnO_2 for the total oxidation of propane. *CrystEngComm* **2015**, *17*, 3005–3014. [CrossRef]
40. Li, Q.; Gu, H.; Li, P.; Zhou, Y.; Liu, Y.; Qi, Z.; Xin, Y.; Zhang, Z. In situ IR studies of selective catalytic reduction of NO with NH_3 on Ce-Ti amorphous oxides. *Chin. J. Catal.* **2014**, *35*, 1289–1298. [CrossRef]
41. Wang, W.; McCool, G.; Kapur, N.; Yuan, G.; Shan, B.; Nguyen, M.; Graham, U.M.; Davis, B.H.; Jacobs, G.; Cho, K.; et al. Mixed-phase oxide catalyst based on Mn-mullite (Sm, Gd)Mn_2O_5 for NO oxidation in diesel exhaust. *Science* **2012**, *337*, 832–835. [CrossRef] [PubMed]
42. Xin, Y.; Li, H.; Zhang, N.; Li, Q.; Zhang, Z.; Cao, X.; Hu, P.; Zheng, L.; Anderson, J.A. Molecular-Level Insight into Selective Catalytic Reduction of NO_x with NH_3 to N_2 over a Highly Efficient Bifunctional Va-MnO_x Catalyst at Low Temperature. *ACS Catal.* **2018**, *8*, 4937–4949. [CrossRef]
43. Kong, M.; Liu, Q.; Zhou, J.; Jiang, L.; Tian, Y.; Yang, J.; Ren, S.; Li, J. Effect of different potassium species on the deactivation of V_2O_5-WO_3/TiO_2 SCR catalyst: Comparison of K_2SO_4, KCl and K_2O. *Chem. Eng. J.* **2018**, *348*, 637–643. [CrossRef]
44. Zhu, M.; Lai, J.K.; Tumuluri, U.; Wu, Z.; Wachs, I.E. Nature of Active Sites and Surface Intermediates during SCR of NO with NH_3 by Supported V_2O_5-WO_3/TiO_2 Catalysts. *J. Am. Chem. Soc.* **2017**, *139*, 15624–15627. [CrossRef] [PubMed]
45. Hu, X.; Shi, Q.; Zhang, H.; Wang, P.; Zhan, S.; Li, Y. NH_3-SCR performance improvement over Mo modified Mo(x)-MnO_x nanorods at low temperatures. *Catal. Today* **2017**, *297*, 17–26. [CrossRef]